

Quantitative Ultrashort Echo Time Imaging for Assessment of Massive Iron Overload at 1.5 and 3 Tesla

Axel J. Krafft,^{1,2} Ralf B. Loeffler,¹ Ruitian Song,¹ Aaryani Tipirneni-Sajja,¹ M. Beth McCarville,¹ Matthew D. Robson,³ Jane S. Hankins,⁴ and Claudia M. Hillenbrand^{1*}

Purpose: Hepatic iron content (HIC) quantification via transverse relaxation rate ($R2^*$)-MRI using multi-gradient echo (mGRE) imaging is compromised toward high HIC or at higher fields due to the rapid signal decay. Our study aims at presenting an optimized 2D ultrashort echo time (UTE) sequence for $R2^*$ quantification to overcome these limitations.

Methods: Two-dimensional UTE imaging was realized via half-pulse excitation and radial center-out sampling. The sequence includes chemically selective saturation pulses to reduce streaking artifacts from subcutaneous fat, and spatial saturation (sSAT) bands to suppress out-of-slice signals. The sequence employs interleaved multi-echo readout trains to achieve dense temporal sampling of rapid signal decays. Evaluation was done at 1.5 Tesla (T) and 3T in phantoms, and clinical applicability was demonstrated in five patients with biopsy-confirmed massively high HIC levels (>25 mg Fe/g dry weight liver tissue).

Results: In phantoms, the sSAT pulses were found to remove out-of-slice contamination, and $R2^*$ results were in excellent agreement to reference mGRE $R2^*$ results (slope of linear regression: 1.02/1.00 for 1.5/3T). UTE-based $R2^*$ quantification in patients with massive iron overload proved successful at both field strengths and was consistent with biopsy HIC values.

Conclusion: The UTE sequence provides a means to measure $R2^*$ in patients with massive iron overload, both at 1.5T and 3T. *Magn Reson Med* 78:1839–1851, 2017. © 2017 Wiley Periodicals, Inc.

Key words: ultrashort echo time imaging; UTE; transfusional iron overload; half-pulse excitation; $T2^*$ quantification; liver MRI

INTRODUCTION

Iron overload is a severe complication arising from multiple blood transfusions and increased intestinal absorption (1–3). Hematologic disorders such as β -thalassemia major and sickle cell anemia require frequent therapeutic blood transfusions to prevent disease complications (4,5). Because there is no physiologic mechanism for iron excretion, repeated transfusions cause an accumulation of iron in several organs, most notably in the liver (6,7), which can lead to substantial morbidity due to iron toxicity (8,9). Therefore, accurate assessment of the hepatic iron content (HIC) is essential for disease management and monitoring of treatment response to iron chelation therapy.

Hepatic iron content has traditionally been monitored by analyzing the iron content of samples from liver biopsies. Noninvasive HIC quantification utilizing MRI has been successfully developed recently (10), eliminating the risks involved with liver biopsies (ie, bleeding and pain) (11). One of these noninvasive MRI methods assesses HIC by quantifying the effective transverse relaxation rate $R2^*$ ($=1/T2^*$) of liver tissue via evaluation of the exponential signal decay seen in multi-echo gradient echo (mGRE) MRI. Previous biopsy-calibrated studies at 1.5 Tesla (T) have shown an excellent linear correlation between HIC and $R2^*$, with a high precision for HIC levels up to 20 to 25 mg Fe/g dry weight (=mg of Fe per g of dry weight liver tissue) (12–15). For HIC levels >25 mg Fe/g dry weight (termed as *massive iron overload* throughout this article), $R2^*$ -based iron assessment suffers a lack in precision and might eventually even fail (10,13,14) because the employed mGRE techniques are intrinsically limited when detecting rapidly decaying MR signals. This aspect becomes even more pronounced at field strengths of 3T and above because $R2^*$ increases linearly with B_0 (approximately twofold increase from 1.5T to 3T) (16–18). Conventional mGRE techniques start to become degraded when measuring signals with $T2^*$ times of 1 ms or less, corresponding to HIC levels above approximately 25 mg Fe/g dry weight at 1.5T (13–15). This limitation of conventional mGRE imaging restricts the current, clinically accessible HIC range at 3T to about 12.5 mg Fe/g dry weight and lower.

These limitations of mGRE-based HIC estimation could be overcome by using ultrashort echo time (UTE) imaging (19), which allows for very short delays ($\leq 100\ \mu\text{s}$) between signal excitation and data acquisition and enables the detection of tissues with very short transverse relaxation times, for example, as demonstrated in

¹Department of Diagnostic Imaging, St. Jude Children's Research Hospital, Memphis, Tennessee, USA.

²Department of Radiology, Medical Physics, Medical Center — University of Freiburg, Faculty of Medicine, University of Freiburg, Freiburg, Germany.

³OCMR, Radcliffe Department of Medicine, University of Oxford, Oxford, United Kingdom.

⁴Department of Hematology, St. Jude Children's Research Hospital, Memphis, Tennessee, USA.

*Correspondence to: Claudia M. Hillenbrand, PhD, Department of Diagnostic Imaging, St. Jude Children's Research Hospital, 262 Danny Thomas Place, MS 220, Memphis, TN, 38105. E-mail: claudia.hillenbrand@stjude.org.

This study was supported by NIH grant 5R01 DK088988 from the National Institute of Diabetes and Digestive and Kidney Diseases (NIDDK) and ALSAC, the fund-raising organization of St. Jude Children's Research Hospital.

Received 2 June 2016; revised 30 November 2016; accepted 1 December 2016

DOI 10.1002/mrm.26592

Published online 16 January 2017 in Wiley Online Library (wileyonlinelibrary.com).

© 2017 International Society for Magnetic Resonance in Medicine

pulmonary and musculoskeletal applications (19–24). Here, UTE sequences have not only been used for basic imaging of such tissues but also to quantitatively characterize the short T2* properties of, for example, lung parenchyma, cortical bone, ultrashort T2 components in white matter, and iceball formation during cyroablation (21,24–30). Moreover, a study by Chappell et al. (31) on the feasibility of UTE imaging in hepatic diseases, such as cirrhosis, hemochromatosis, fibrosis, and hepatocellular carcinomas, already showed the general applicability of UTE-based T2* measurements in iron overload. However, this study did not aim at a specific investigation of UTE imaging in massive HIC settings, as reflected by the reported mean T2* time of 7 ms (standard deviation (SD) 2.7 ms) for patients showing patterns of hemochromatosis. According to three independently performed, biopsy-calibrated R2*-HIC conversions (13–15), T2* times from 4 to 10 ms would translate into HIC values from about 2.3 to 6.6 mg/g dry weight, which still is within a range that can be clinically assessed via mGRE imaging (10,13–15). Nevertheless, the study by Chappell et al. (31) demonstrates the potential of UTE imaging in iron overload assessment.

Chappell et al., as well as other studies on UTE-based T2* assessment, employ slice-selective 2D UTE imaging (24–31), which can be achieved via half-sinc radiofrequency (RF) pulse excitation in combination with center-out radial sampling (19,32,33). Half-pulse excitation requires two acquisitions with respectively inverted slice-selection gradients but otherwise identical scan parameters, which are combined in the complex domain to obtain the desired slice profile. The combination of two half-pulse acquisitions with inverted slice-selection gradients theoretically should lead to a full cancellation of signals from out-of-slice locations (19,32,33). Unfortunately, this mechanism is sensitive to any system imperfections affecting the slice-selection gradient, such as eddy currents or gradient delays (34). Such imperfections can manifest in insufficient cancellation of unwanted out-of-slice signals (29,30,35–37), which hampers quantitative imaging as needed for R2*-based HIC assessment (24–30).

Here, we describe the technical implementation of a 2D UTE sequence that is specifically applicable for hepatic T2* quantitation whenever conventional mGRE techniques become imprecise due to T2* shortening: patients with high or massive HIC and at higher field strengths. We systematically studied confounding factors and integrated simple, readily available sequence modules to largely avoid unwanted effects hampering T2* quantitation in such situations. The sequence employs spatial saturation (sSAT) bands to reduce unwanted out-of-slice signal contributions and achieves dense temporal sampling of the rapidly decaying signal, as seen for massive HIC, via the acquisition of interleaved echo trains without requiring breath-holding. The sequence was tested and quantitatively evaluated in phantom experiments and *in vivo*.

METHODS

Sequence Concept and Implementation

Our 2D UTE sequence uses half-sinc RF pulse excitation (pulse duration = 1.0 ms, time-bandwidth product = 2.0),

together with center-out radial sampling (19,20,32,33) including data acquisition during ramp-up of the readout gradient. To minimize the delay between RF excitation and data acquisition, the half-sinc pulse shape is modified via variable-rate selective excitation (38) to account for the time-varying gradient amplitude during ramp-down of the slice-selection gradient. The two half-pulse acquisitions with respectively inverted slice-selection gradients are sampled consecutively (as inner averages) to directly combine the data in the complex domain.

Improved 2D UTE slice selectivity by suppression of unwanted out-of-slice signal contributions has been demonstrated via quadratic phase sSAT pulses (36). Similar to this concept, we added readily available, conventional truncated sinc-shaped sSAT pulses for out-of-slice signal suppression to the 2D UTE sequence. The sSAT pulses (pulse duration = 2.56 ms, time-bandwidth product = 8.0) were applied in each repetition time (TR) interval prior to half-pulse excitation so that saturation bands were induced on both sides and in parallel with the UTE imaging slice.

Because 2D UTE imaging employs radial sampling, the images are prone to streaking artifacts that can emerge from bright signal intensities in the periphery of the image (39). Such high peripheral signal intensities can arise from subcutaneous fat in mGRE imaging protocols, especially when surface coils are used for optimized signal reception, as done in abdominal imaging. To avoid high signal intensities from fat, fat suppression via chemically selective saturation (CHESS) (40) RF pulses was incorporated. The Gaussian CHESS pulses (duration = 10.24/5.12 ms, off-resonance = 187.5/375 Hz at 1.5 T/3 T) were also applied in each TR interval prior to the half-pulses.

The sequence uses a multi-echo readout gradient with readout rewinding to acquire multiple echoes, as needed, for T2*/R2* quantification. All echoes are sampled as half echoes, including ramp sampling identical to the first (UTE) echo. As shown in other UTE applications (eg, in cortical bone (25,26)), dense echo sampling is required to accurately capture the rapid signal decay for tissues with very short T2* times. Therefore, additional UTE echoes need to be acquired, which was accomplished by acquisition of additional multi-echo readout trains that are shifted by small echo-time increments ΔTE relatively to the first echo train. The radial sampling process of the UTE sequence is intrinsically insensitive to motion artifacts (41) and does not necessarily require breath-holding, as opposed to Cartesian acquisition schemes. Our UTE acquisition scheme exploits this fact to acquire additional, interleaved multi-echo trains in free-breathing. A schematic of the free-breathing interleaved multi-echo UTE (FB-imUTE) sequence is illustrated in Figure 1.

Images were reconstructed via inverse Fourier transformation after re-gridding of the radially collected data to a Cartesian grid using a Kaiser-Bessel kernel (42,43). The sequence and image reconstruction were implemented on 1.5T and 3T scanners (Magnetom Avanto and Trio, Siemens Healthcare, Erlangen, Germany). Prior to experimental validation in phantoms and initial *in vivo* testing, remaining image distortions, which can emerge in

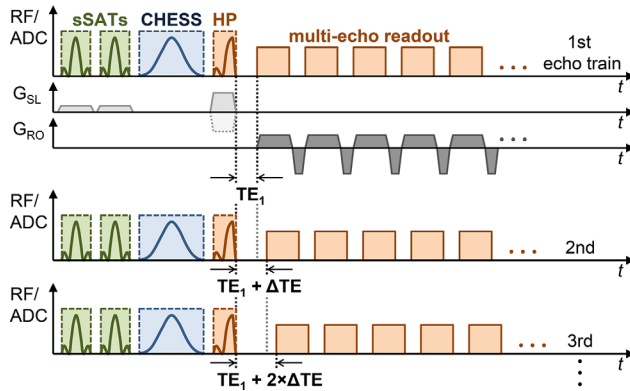


FIG. 1. Schematic excitation and acquisition diagram of the free-breathing interleaved multi-echo UTE sequence; only important elements are shown: Prior to each half-pulse excitation, CHESS pulses for fat suppression and sSAT pulses for out-of-slice signal suppression are applied. CHESS and sSAT pulses are followed by spoiler gradients (not shown) to dephase transverse magnetization. The sSAT bands are oriented parallel to the imaging slice. The slice selection gradient G_{SL} (light gray; dotted line indicates alternating polarity of slice-selection gradients) and readout gradient G_{RO} (dark gray) are illustrated for the first echo train only. Each echo of the multi-echo readout train is acquired via center-out radial sampling including data acquisition during ramp-up of the readout gradients. The sequence acquires additional echo trains, which are shifted relative to the previous echo train by a small echo-time increment ΔTE to achieve dense temporal sampling even for fast $T2^*$ decay. ADC, analog-to-digital converter; CHESS, chemically selective saturation pulses; G_{RO} , readout gradient; G_{SL} , slice selection gradient; HP, half-pulse; RF, radiofrequency; sSAT, spatial saturation; TE, echo time.

radial acquisitions due to temporal delays between readout gradients and data acquisition in the analog-to-digital converter (ADC) (44), were investigated and corrected in a series of prescans. The correction parameters and sequence parameters affecting readout gradient and ADC timing (eg, pixel bandwidth and number of data points per ADC) remained unchanged during all subsequent phantom and in vivo measurements; thus, the prescans had to be executed only once for each scanner at the very beginning of this study (please refer to Supporting Figures S1 and S2 for details).

For all $T2^*$ -weighted, multi-echo image series (ie, phantom and in vivo measurements), pixel-wise $T2^*$ fitting was done via a nonlinear least square fit of the second moment of the gradient echo signal (45) implemented in MatLab (MathWorks, Natick, MA). The second moment considers the expectation value of the squared magnitude signal S_M^2 , which is fitted to the equation $S_M^2 = S^2 + N^2$, where S denotes the ideal, noise-free monoexponentially decaying signal and N reflects noise. In comparison to the expectation value of the plain magnitude signal S_M , the second moment fit has a much simpler form and was therefore implemented here (45).

Phantom Measurements

In a series of phantom measurements, the effect of out-of-slice signal contributions on $T2^*/R2^*$ quantification

was assessed. A cylindrical phantom bottle ($V = 500 \text{ mL}$) filled with a 2% agar-water solution (Sigma-Aldrich, St. Louis, MO), which was doped with iron nanoparticles (BNF-Starch particles, diameter = 80 nm, micromod Partikeltechnologie GmbH, Rostock, Germany; Fe concentration = 13.75 $\mu\text{g/mL}$), was placed inside the system's head coil in the iso-center of the magnet bore with the symmetry axis of the phantom bottle in parallel to B_0 . A second, larger cylindrical phantom bottle ($V = 1,000 \text{ mL}$) filled with pure 2% agar-water solution was positioned right behind the smaller bottle so that the larger bottle was located approximately 3 cm off the magnet's iso-center (schematic illustration given in Figure 2). Overall, three multi-echo image series were acquired at the iso-center in axial slice orientation. Two image series were acquired with the 2D multi-echo UTE (mUTE) sequence without and with sSAT bands, respectively; in addition, one image series was measured with a conventional mGRE sequence serving as reference for $T2^*/R2$ quantitation (14). The following image parameters were used for the 2D mUTE sequences without and with sSAT bands: TR/TE₁ = 52.5/0.1 ms; 12 echoes; echo spacing (ESP) = 1.8 ms; field of view (FOV) = 250 × 250 mm²; slice thickness (SL) = 10 mm; 192 radial spokes, 192 points per spoke; pixel bandwidth (BW) = 780 Hz/px; flip angle (FA) = 20°; sSAT band parameters: sSAT band thickness = 100 mm; gap to imaging slice = 10 mm (ie, equivalent to slice thickness); total acquisition time (TA) ≈ 20 s. No CHESS pulses and no additional ΔTE -shifted echo trains were applied in the mUTE acquisitions in these phantom measurements. The mGRE sequence was applied with the following parameters: TR/TE₁ = 200/1.1 ms, 20 echoes, ESP = 1.6 ms, FOV = 250 × 250 mm², SL = 10 mm, matrix = 128 × 128, BW = 1,950 Hz/px, FA = 35°; TA ≈ 25 s.

In a second series of phantom measurements, the FB-imUTE sequence was evaluated for correct $T2^*/R2^*$ quantitation using a mGRE sequence as reference. Ten cylindrical phantom bottles ($V = 500 \text{ mL}$) were filled with 2% agar-water solution and doped with iron nanoparticles of different concentrations (BNF-Starch particles, diameter = 80 nm, micromod Partikeltechnologie GmbH, Rostock, Germany; range of Fe concentrations in phantoms = 0.4–220 $\mu\text{g/mL}$) to cover a wide range of $T2^*/R2^*$ values reflecting low to massive HIC conditions. Axial images were acquired for each phantom individually (each phantom placed inside the system's head coil in the magnet's iso-center) using the FB-imUTE sequence, including CHESS and sSAT pulses and a mGRE protocol based on a previously published, biopsy-calibrated mGRE sequence for HIC assessment (14). The FB-imUTE sequence parameters were as described above, except that five interleaved echo trains with ΔTE shifts of 0.25 ms were used (TA ≈ 1:40 min). The mGRE sequence parameters were also as described above, except that signal averaging (number of averages = 5) was used to achieve a sufficiently high signal-to-noise ratio (SNR), even for phantoms with very short $T2^*$ times. Axially oriented multi-echo images (slice location in iso-center) were collected at 1.5T and 3T.

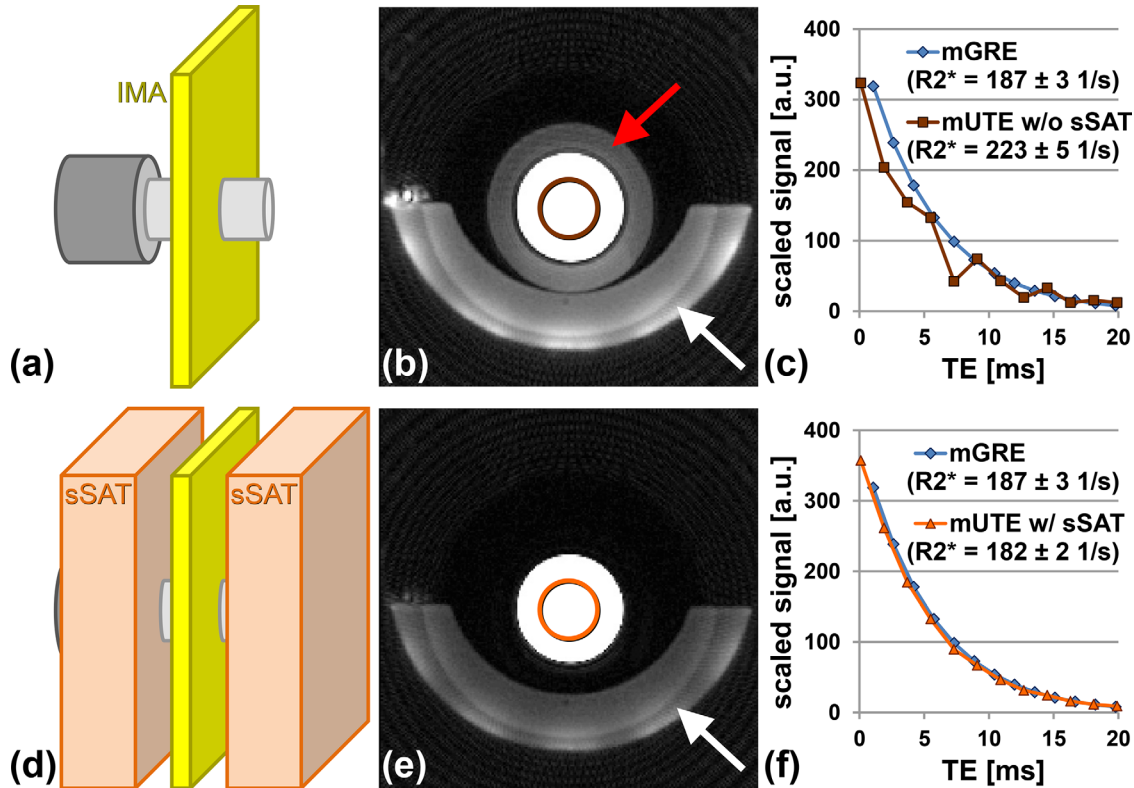


FIG. 2. Effect of sSAT bands to suppress unwanted out-of-slice signals. (a,d) Schematic (dimensions not to scale) of experimental setup (IMA indicates imaging slice, sSAT indicates sSAT band) with two phantom bottles (light and dark gray) placed one behind the other. Axial UTE images (b) without and (e) with sSATs. Substantial out-of-slice signals from the larger phantom positioned behind the smaller phantom bottle can be seen (red arrow). Signal below the phantom bottle (white arrows) arises from cushion used for positioning of the phantoms. T2* decay seen for averaged signal at the center (circles) of the phantom bottle for the mUTE (c) without and (f) with sSAT pulses. For comparison, the signal decay measured with a reference mGRE sequence also is shown (mGRE images not shown). Without sSATs, the out-of-slice signals lead to distortions of the signal decay hampering T2* analysis. Mean R2* values and standard deviation for each acquisition are given in the plot legend. mGRE, multi-gradient echo; mUTE, multi-echo ultrashort echo time; sSAT, spatial saturation; R2*, transverse relaxation rate; TE, echo time.

In Vivo Testing

In vivo testing of the UTE sequence was done on 1.5T and 3T platforms in a total of seven subjects with iron overload. Participants had a history of >12 cumulative packed red-blood cell transfusions, and all were consented to participate in a prospective institutional review board-approved study on iron overload assessment (www.clinicaltrials.gov, NCT01572922).

For all scans, subjects were placed on the patient table in a supine position and positioned so that the liver was located in the iso-center of the magnet. Imaging slices were positioned at the location of the main portal vein and acquired in axial-slice orientation with body array and spine array coils. Prior to the acquisition of any UTE and GRE images, the system's *standard* shim procedure was executed.

To study the reduction of streaking artifacts, two subjects were scanned using single breath-hold (BH) multi-echo UTE acquisitions (BH-mUTE) including sSAT bands without and with CHESS pulses, respectively. The BH-mUTE images were acquired with sequence and sSAT parameters as described above (Phantom Measurements section) without additional ΔTE-shifted echo trains (TA ≈ 20 s).

The in vivo applicability of the FB-imUTE sequence for T2*/R2* quantification in the presence of massive iron overload was tested in five subjects with clinically anticipated massive HIC, four diagnosed with sickle cell disease and one with Diamond-Blackfan anemia. The lifetime cumulative number of packed red blood cell units was ≥ 90 for all five subjects. FB-imUTE images were acquired during regular breathing. The sequence parameters were as described in the section phantom measurements, except that the FOV was adjusted individually for each subject (FOV = 400 × 400/420 × 420 mm²; TA ≈ 1:40 min). For comparison, the scan protocol also included BH-mUTE acquisitions, without additional ΔTE-shifted echo trains but including sSAT bands and CHESS pulses (sequence parameters as given above, with FOV set identical to FB-imUTE; TA ≈ 20 s). For reference, subjects also received scans with a R2*-HIC biopsy-calibrated, single BH-mGRE sequence, as previously described (14). The mGRE sequence parameters were also as described in the Phantom Measurements section, except that a bipolar readout gradient scheme was employed to achieve a shorter ESP of 0.8 ms and a rectangular FOV (FOV = 340 × 276/320 × 260 mm², matrix = 128 × 104; TA ≈ 21 s) was chosen.

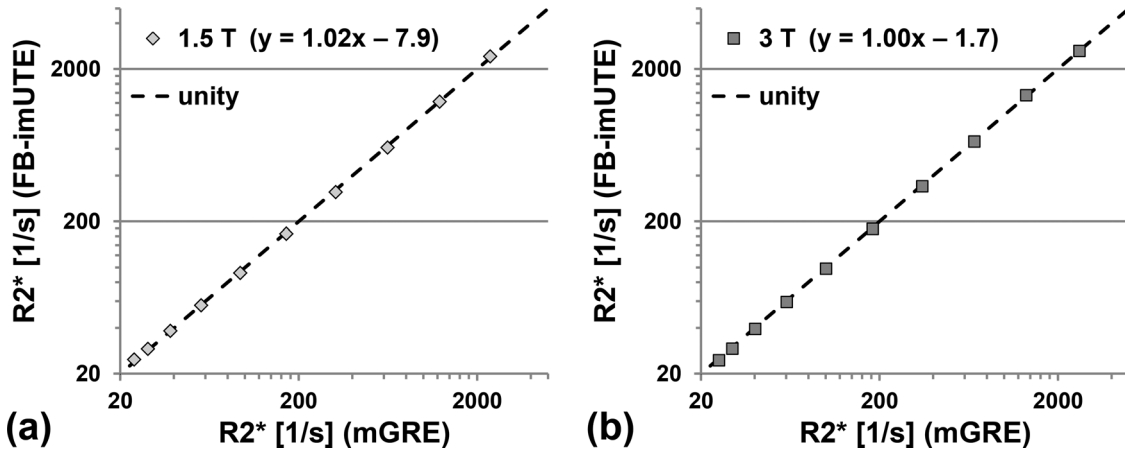


FIG. 3. Results of $R2^*$ measurements in phantoms doped with iron nanoparticles at different concentrations for (a) 1.5T and (b) 3T. $R2^*$ values were measured with the proposed FB-imUTE sequence and compared to a reference mGRE acquisition. Five averages were done for the mGRE sequence to achieve sufficient signal-to-noise ratio for reliable $R2^*$ assessment in the phantoms with high iron-particle concentration. Linear regression (results given in plot legend) shows that both sequences yield highly consistent $R2^*$ results for both field strengths across a large dynamic range. mGRE, multi-gradient echo; FB-imUTE, free-breathing multi-echo ultrashort echo time; $R2^*$, transverse relaxation rate; T, Tesla.

For each acquisition, the mean hepatic $R2^*$ value was obtained from the mean value within a manually drawn whole liver region of interest (ROI) after pixel-wise $T2^*/R2^*$ mapping, as described above. Any unwanted structures, such as blood vessels, were excluded based on a histogram analysis (46).

RESULTS

Phantom Testing

Unwanted out-of-slice signal contributions affect $T2^*/R2^*$ extraction from 2D multi-echo UTE imaging, as illustrated in Figure 2. Without sSAT bands, substantial signal contributions from the larger phantom located outside the imaging slice are visible (Fig. 2b). Application of the sSAT pulses removes these unwanted signal contributions (Fig. 2e). In addition to the erroneous background signal intensities, the out-of-slice signal contributions also induce distortions in the measured signal decay, which impact the measured $R2^*$ values ($R2^*$ GRE vs. $R2^*$ UTE without sSAT = 187 ± 3 1/s vs. 223 ± 5 1/s) (Fig. 2c). A smoother, mono-exponential signal decay without signal distortions was found in the UTE acquisition with sSAT pulses, which substantially improves the $R2^*$ result ($R2^*$ GRE vs. $R2^*$ UTE with sSAT = 187 ± 3 1/s vs. 182 ± 2 1/s) (Fig. 2f).

The systematic comparison of the FB-imUTE and mGRE $R2^*$ results in phantoms with iron nanoparticles (approximate range of $R2^*$ values at 1.5/3 T = 20–2,420/30–2,640 1/s) shows that the proposed UTE sequence yields $R2^*$ values, which are consistent with the results from the mGRE reference sequence (linear regression results at 1.5/3 T: $y = 1.02x - 7.9/1.00x - 1.7$) (Fig 3). $R2^*$ quantitation improved at both field strengths for FB-imUTE relative to mGRE imaging with increasing iron concentration. For example, an approximately threefold reduction of the SD of the $R2^*$ values was observed in the phantom with the highest iron concentration (SD of

$R2^*$ values at 1.5T and 3T: ± 296 1/s and ± 167 1/s for mGRE, and ± 101 1/s and ± 55 1/s for FB-imUTE).

In Vivo Testing

In vivo tests of the BH-mUTE protocols with and without CHESS pulses showed a reduction of streaking artifacts from bright peripheral subcutaneous fat signal by the application of CHESS (Fig. 4). Streaking artifacts are not only visible in the magnitude images (Figs. 4a/d) but also in the associated $T2^*$ maps leading to systematically larger $T2^*$ values compared to image regions where no streaking artifacts are present (Figs. 4g,h).

Figure 5 summarizes the 1.5T results from the measurements with the BH-mGRE, the BH-mUTE, and the proposed FB-imUTE sequence in the five subjects with massive iron overload, as confirmed by post-MRI liver biopsy with HIC values ranging from 25.4 to 35.4 mg Fe/g dry weight (mean $HIC \pm SD = 29.6 \pm 3.3$ mg/g dry weight). Figure 6 depicts signal-versus-TE plots, as measured in circular hepatic ROIs with the BH-mGRE, BH-mUTE, and FB-imUTE sequences. In comparison to the BH-mGRE and BH-mUTE acquisitions, the FB-imUTE sequence did not yield a substantially higher SNR at the time point of TE_1 but provided a denser temporal sampling of the rapid signal decay, which improves $T2^*/R2^*$ quantitation. For the FB-imUTE sequence, an approximately twofold smaller $R2^*$ SD was found in comparison to the BH-mGRE data. Figure 5 also highlights the motion insensitivity of the FB-imUTE sequence: no additional artifacts from breathing motion can be seen in the free-breathing UTE images (Figs. 5k-o) in comparison to the breath-hold UTE images (Figs. 5f-j).

The results from the application of the FB-imUTE sequence at 3T are shown in Figures 7 and 8. Because hepatic $R2^*$ values increase approximately linearly with B_0 for patients with iron overload (16–18), the associated $T2^*$ decay for the five cases with massively high HIC is too fast to be captured sufficiently well with BH-mGRE

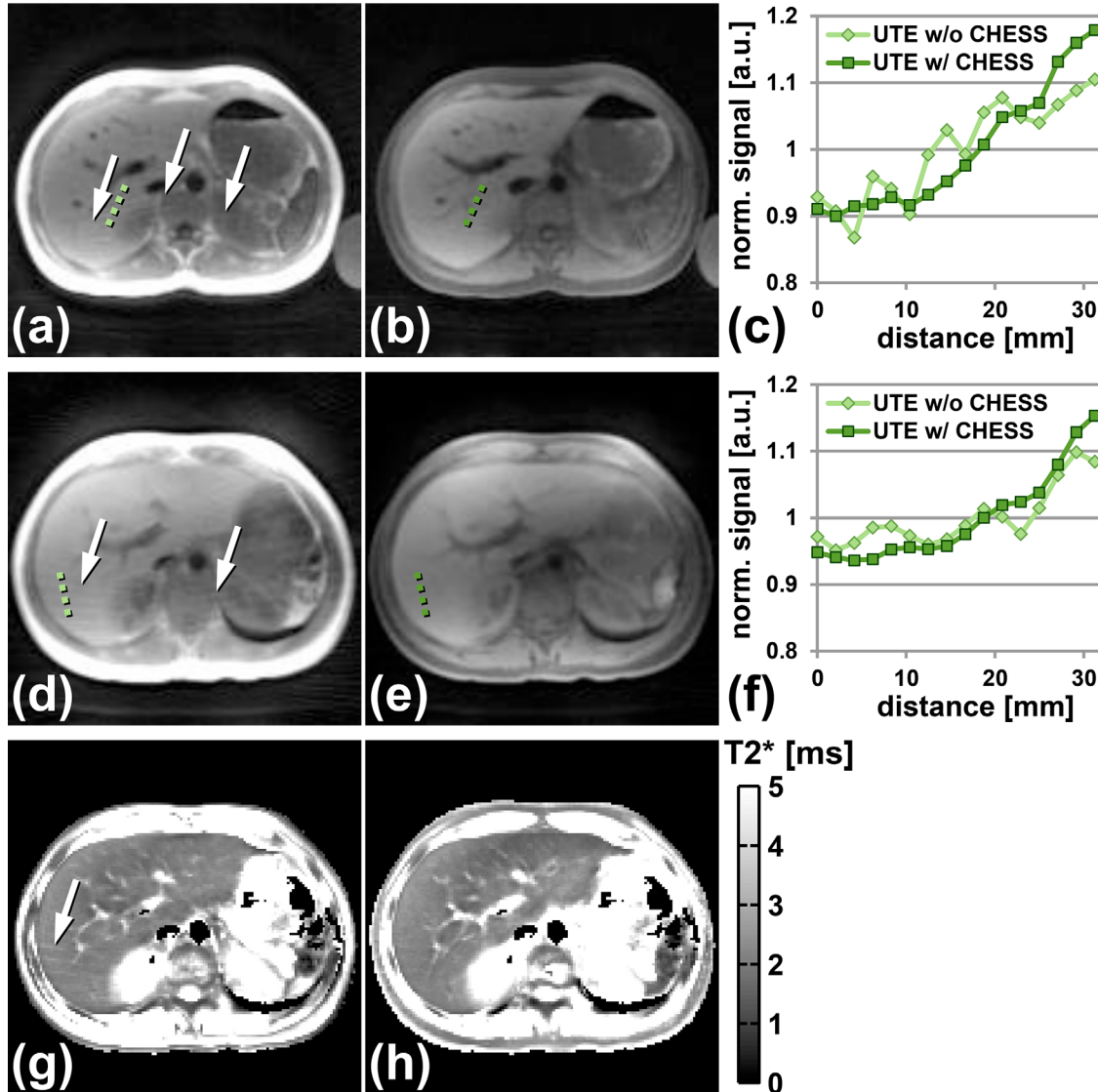


FIG. 4. Effect of CHESS pulses to suppress bright signal intensities in peripheral subcutaneous fat tissue. BH-mUTE images without CHESS at (a) 1.5T and (d) 3T show substantial streaking artifacts (white arrows). (b,e) Corresponding UTE images with CHESS pulses. Streaking artifacts are substantially reduced for both field strengths. The graphs in (c) and (f) reflect plots of normalized signal intensities along the green dotted lines given in (a,b) and (d,e), respectively. Without CHESS, the signal intensities show an oscillatory pattern that almost is absent in the UTE images with CHESS. The streaking artifacts also affect T2* mapping, as shown exemplarily for the 3T data, where streaking artifacts can be seen in T2* maps (g) without CHESS in contrast to T2* maps (h) with CHESS.

BH-mUTE, breath-hold multi-echo ultrashort echo time; CHESS, chemically selective saturation pulses; mGRE, multi-gradient echo; T, Tesla.

acquisitions. T2* maps retrieved from the mGRE images (Figs. 7a-e) appear very noisy, and the histogram plots of T2* values (Fig. 8) found within the liver parenchyma after exclusion of unwanted structures appear almost flat, which prevents a reliable hepatic R2* assessment. Although the T2* maps extracted from the BH-mUTE images (Figs. 7f-j) appear less noisy, the precision of T2*/R2* assessment also is limited, as can be seen from the histogram analysis (Fig. 8): the BH-mUTE T2* values are distributed over a wide range, displaying a broader maximum at higher T2* values. In contrast, T2* maps extracted from the FB-imUTE acquisitions appear smooth within the entire liver parenchyma. For all five subjects, the T2* histogram plots show a well-defined, sharp maximum enabling a representative measurement

of mean hepatic R2* values. Mean hepatic R2* values ranging from about 1,500 to 3,200 1/s were found with relative errors from about ± 9 to $\pm 26\%$ (relative error = SD/mean), respectively.

DISCUSSION

We present the development and implementation of a 2D UTE imaging sequence for hepatic T2*/R2* assessment in massive hepatic iron overload at 1.5T and 3T. In such conditions, established mGRE techniques for R2*-based HIC estimation are limited or might even fail due to the rapidly decaying signals (10,13,14). The FB-imUTE sequence overcomes this limitation by providing dense temporal sampling of the fast signal decay at

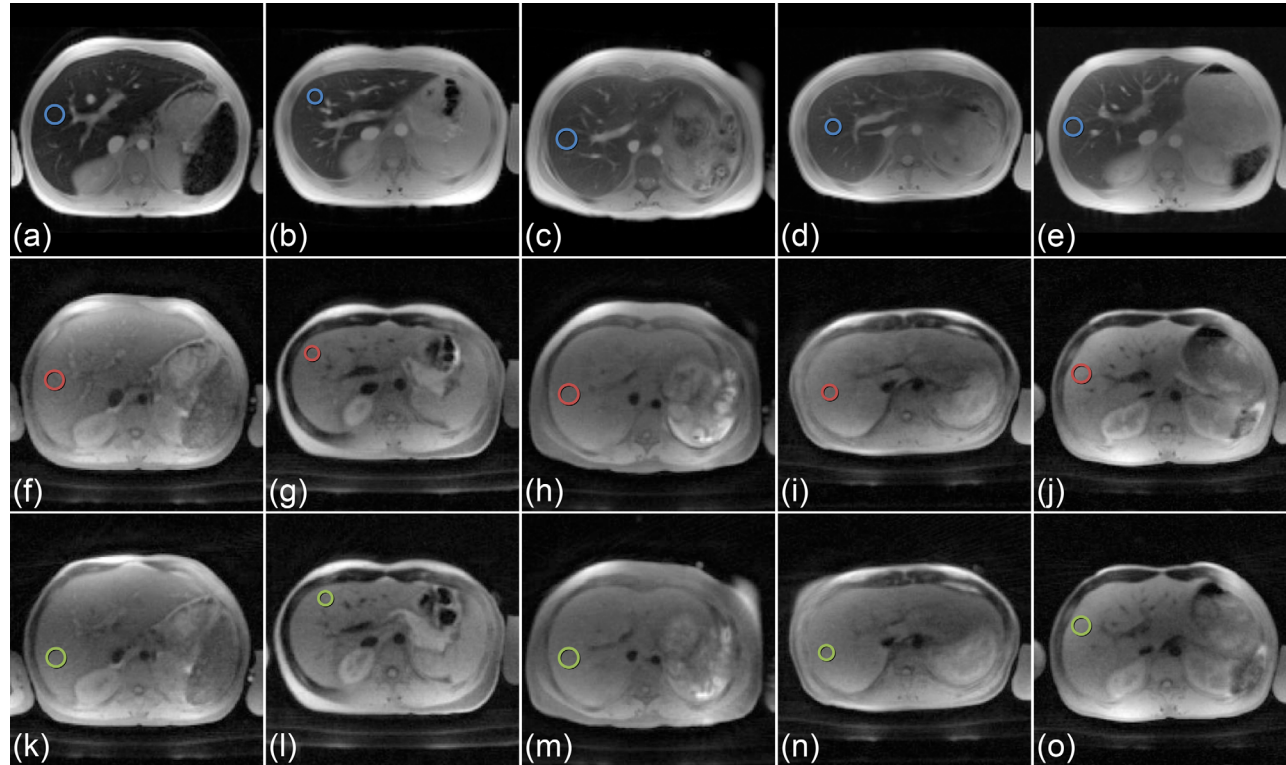


FIG. 5. In vivo imaging with the BH-mGRE, BH-mUTE, and FB-imUTE sequences in the five subjects with massive HIC at 1.5 Tesla. Images acquired at first echo time with the (a-e) conventional BH-mGRE ($TE_1 = 1.1$ ms), with the (f-j) BH-mUTE ($TE_1 = 0.1$ ms), and with the (k-o) FB-imUTE ($TE_1 = 0.1$ ms) sequence. The two UTE sequences were applied with sSAT bands and chemically selective saturation pulses, as described. Barely any additional artifacts due to breathing motion can be seen in the free-breathing acquisitions (k-o) in comparison to the breath-hold acquisitions (a-j). Blue, red, and green circles indicate regions of interest, which were used to illustrate the signal decays given in Figure 6.

BH-mGRE, breath-hold multi-gradient echo; BH-mUTE, breath-hold multi-echo ultrashort echo time; FB-imUTE, free-breathing interleaved multi-echo ultrashort echo time; HIC, hepatic iron content; sSAT, spatial saturation; TE, echo time; UTE, ultrashort echo time.

multiple ultrashort echo times, which is paramount for correct $T2^*/R2^*$ assessment. The sequence was equipped with sSAT bands for an improved slice selectivity of the half-pulse excitation process, and with CHESS pulses for a reduction of streaking artifacts. Otherwise both effects, improper slice selectivity and streaking, would interfere with quantitative imaging.

CHESS pulses were required to minimize streaking artifacts arising from bright peripheral subcutaneous fat signal. The streaking artifacts can be explained by the point-spread-function (47) of radial sampling such that localized, high-signal levels in the periphery of the image partly spread their intensities over the entire image (39,48,49). The streaking artifacts not only emerged in the magnitude images but also translated into erroneous $T2^*/R2^*$ maps (Fig. 4). In comparison to other approaches (48–50), the use of CHESS pulses is appealing as a simple means to reduce streaking for our application. The CHESS pulses have the incidental benefit of reducing fat–water oscillations in the measured signal decay, which otherwise would have to be accounted for by appropriate signal modeling (51,52).

The sSAT pulses were implemented to suppress unwanted signal contributions from imperfect cancellation of out-of-slice signals that otherwise distort the

measured signal decay and severely hamper $T2^*/R2^*$ quantitation (Fig. 2). The out-of-slice contributions not only superimpose the in-slice signal manifesting as a simple offset in the measured signal decay, but introduce modulations in the signal decay, which distort $T2^*/R2^*$ estimation. The observed temporal modulations are consistent with other studies (30,37) in which the authors also report out-of-slice-induced variations in the signal-time course of half-pulse 2D UTE imaging. They can be explained by in- and out-of-phase effects of the out-of-slice contributions to the in-slice signal (37).

The impact of improper slice selectivity of half-pulse excitation due to eddy currents has been reported in other studies on 2D UTE-based $T2^*$ assessment (24–30), and several mechanisms were employed for correction. For example, 2D non-slice-selective approaches, which substitute the half-pulses with short non-selective rectangular pulses and thus eliminate the need for slice-selection gradients, have been successfully used to study $T2^*$ of smaller samples (25). However, such strategies might be disadvantageous for in vivo imaging of the liver because the obtained signal represents an integrated signal over the entire excitation volume. In 2D slice-selective UTE imaging, bipolar slice-selection gradients were implemented to reduce unwanted effects from eddy currents

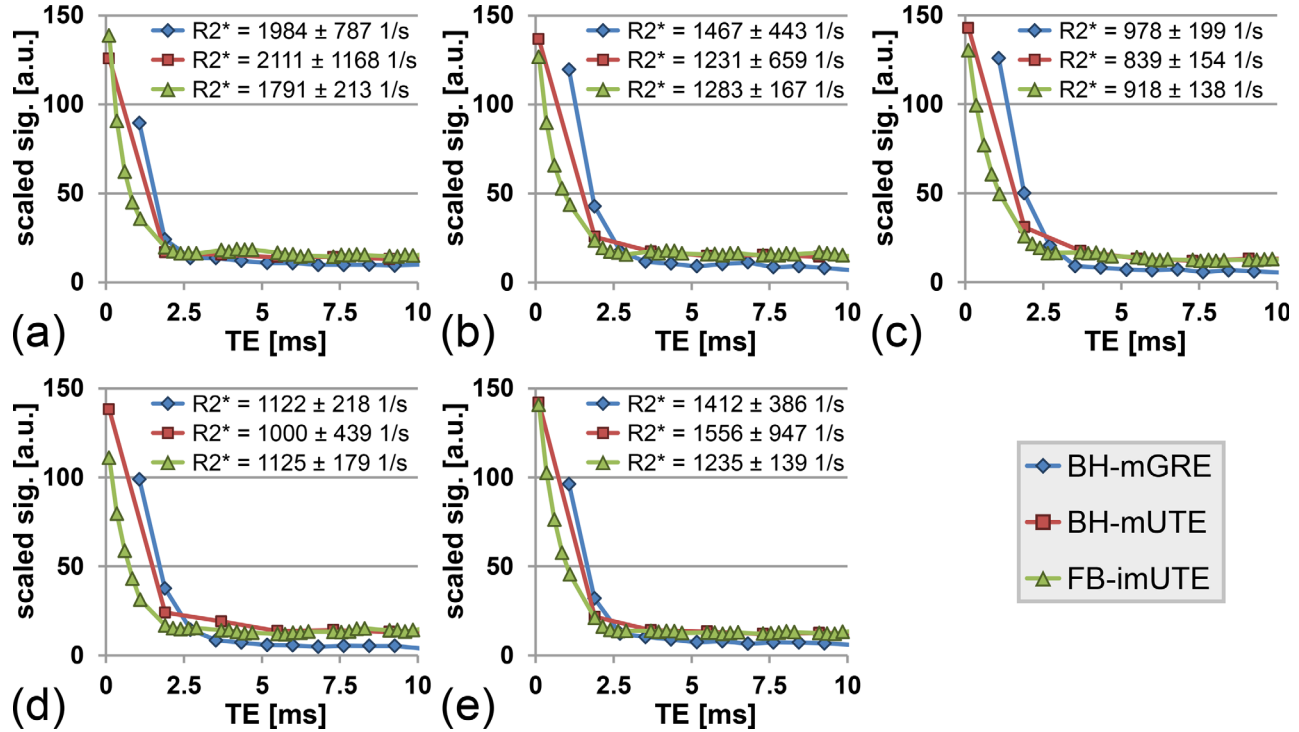


FIG. 6. Signal decays as seen in hepatic regions of interest (blue, red, and green circles in Fig. 5) measured with BH-mGRE, BH-mUTE, and FB-imUTE sequences for the five subjects with massive hepatic iron content at 1.5 Tesla. Note that signal intensities were re-scaled to an intensity range from 0 to 150 for comparison. Whole liver mean $R2^*$ results (mean \pm standard deviation) of each subject are given in the plot legend for each sequence. With the FB-imUTE sequence, additional UTE echoes are acquired, which enables dense sampling of the rapid $T2^*$ decay. The dense temporal sampling of the FB-imUTE sequence improves the $R2^*$ assessment, as can be seen from the reduced standard deviation.

BH-mGRE, breath-hold multi-gradient echo; BH-mUTE, breath-hold multi-echo ultrashort echo time; FB-imUTE, free-breathing interleaved multi-echo ultrashort echo time; $R2^*$, transverse relaxation rate; TE, echo time; UTE, ultrashort echo time.

(24,26–28), and more advanced concepts to apply eddy current compensated slice-selection gradients were presented (29,30). Our strategy to minimize unwanted out-of-slice effects via application of sSAT pulses follows the concept of Josan et al., using quadratic phase pulses to yield an improved half-pulse selectivity (36). Although such pulses offer a sharp saturation profile, they typically require more time than conventional sinc-shaped sSAT pulses and a more complex implementation. As can be seen from our phantom work (Figs. 2 and 3), the implementation of sSAT bands enables accurate $T2^*$ quantitation and therefore might serve as a simple but effective approach to avoid distortions in slice selectivity.

Both, CHESS and sSATs, pulses might affect the $T2^*/R2^*$ estimation. Previous studies have shown an effect of fat suppression on the measured $T2^*/R2^*$ values in patients with transfusional iron overload (53,54), which most likely arises from saturation of off-resonant signal components within the broadened line profile associated with short $T2^*$ times. Similarly, the sSAT pulses also might impact the observed $T2^*/R2^*$ values due to magnetization-transfer effects through saturation of signal from protons bound to the broad macro-molecular pool (37,55). However, no $R2^*$ differences were found in phantoms for mGRE acquisitions and UTE acquisitions employing CHESS and sSAT pulses (Fig. 3). Only minor

$R2^*$ differences were seen at 1.5T for the BH-mGRE and the FB-imUTE sequence for our subjects with massive HIC (Figs. 5 and 6), which should be validated in a larger patient cohort.

Our in vivo $R2^*$ results suggest a multi-echo acquisition that only contains a single UTE image at the beginning of the echo train might not be sufficient to substantially improve $R2^*$ assessment over the established mGRE protocols in massive iron overload: at 1.5 T, the BH-mUTE sequence, which collects all data within a single breath-hold but only acquires a single UTE image at $TE_1 = 0.1$ ms, did not yield a smaller SD of hepatic $R2^*$ values in comparison with a biopsy-calibrated BH-mGRE protocol. Contrary to the BH-mUTE sequence, the FB-imUTE sequence—although acquiring the data in free-breathing—records multiple images with short TEs ($TE_1 < 1$ ms) via ΔTE -shifted, interleaved echo trains which provides dense temporal sampling of the fast decays. This greatly improves the $R2^*$ quantitation via non-linear least square fitting, as seen from the smaller SD of $R2^*$ values. The potential of the FB-imUTE sequence for $R2^*$ quantification in massive iron overload is shown in the in vivo measurements at 3T: only the FB-imUTE data proved successful to reliably quantify mean hepatic $R2^*$ values of up to 3,200 1/s, as can be appreciated from the histogram plots of FB-imUTE $T2^*$ values exhibiting well-defined maxima for

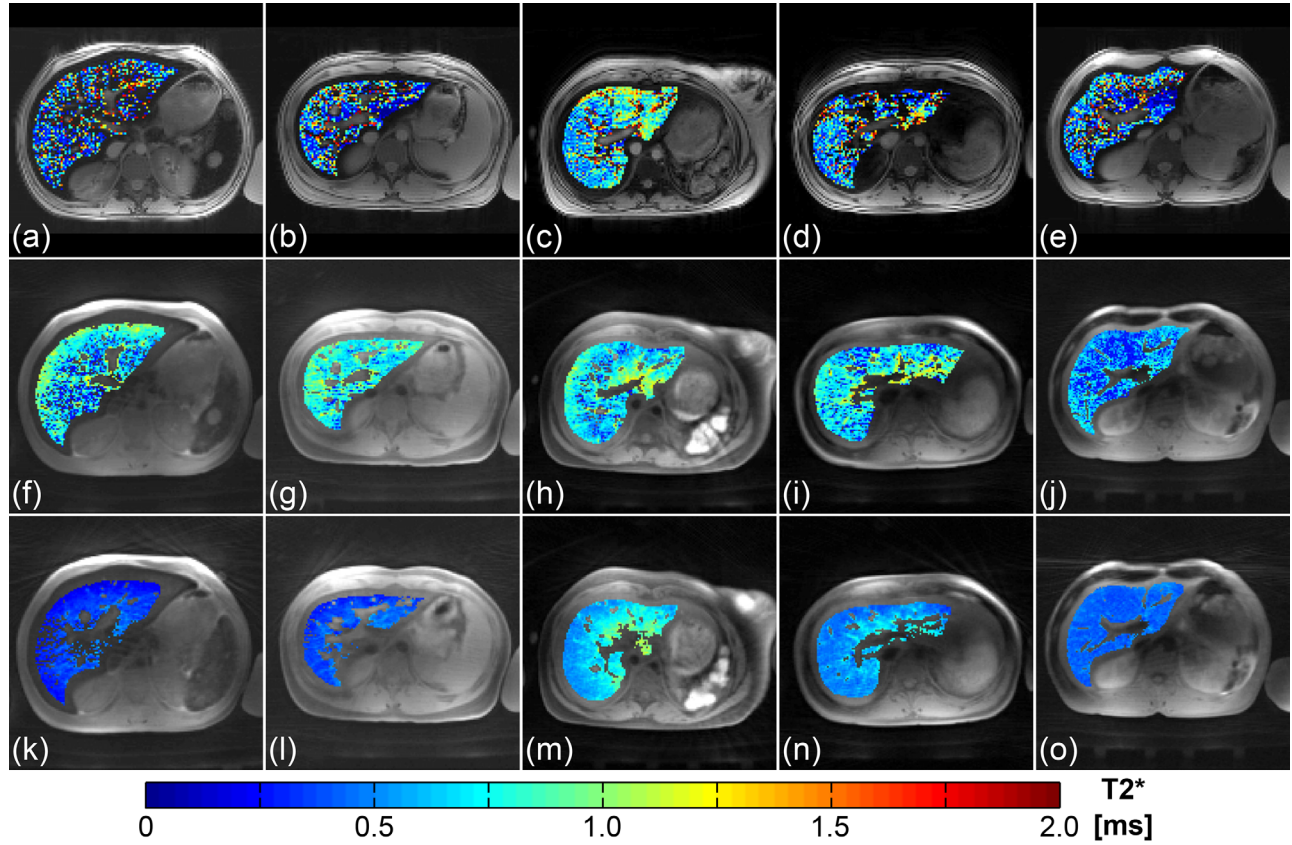


FIG. 7. In vivo imaging with the BH-mGRE, BH-mUTE, and FB-imUTE sequences in the five subjects with massive hepatic iron content at 3 Tesla. Images acquired at first echo time with the (a-e) conventional BH-mGRE ($TE_1 = 1.1$ ms), with the (f-j) BH-mUTE ($TE_1 = 0.1$ ms), and with the (k-o) FB-imUTE ($TE_1 = 0.1$ ms) sequence. The colored overlay represents results from pixel-wise $T2^*$ fitting within the liver parenchyma after exclusion of unwanted structures such as blood vessels.

BH-mGRE, breath-hold multi-gradient echo; BH-mUTE, breath-hold multi-echo ultrashort echo time; FB-imUTE, free-breathing interleaved multi-echo ultrashort echo time; $R2^*$, transverse relaxation rate; TE, echo time.

all five subjects (Fig. 8). The previously established BH-mGRE protocol and the BH-mUTE sequence (single UTE) do not yield a proper hepatic $R2^*$ assessment. Although the $T2^*$ maps derived from the BH-mUTE data appear less noisy compared to the mGRE results, the histogram plots show that the $T2^*$ values are also widely distributed, with a broader peak at longer $T2^*$ times in comparison to the FB-imUTE (Fig. 8). The wide distribution of BH-mUTE- $T2^*$ values could be explained by inaccurate $T2^*$ fitting from BH-mUTE data due to a combination of limited SNR and insufficient temporal sampling of the rapid signal decay. The noisy and widely distributed BH data produce mean $R2^*$ values (cf. plot legend of Fig. 8), which do not appear as meaningful measures of mean hepatic $R2^*$ at 3T. In contrast, the FB-imUTE sequence with its narrow $T2^*$ distributions seems to enable correct assessment of mean hepatic $R2^*$, even at 3T. This is further supported by the fact that only the FB-imUTE data reflect an approximately twofold $R2^*$ increase from 1.5T to 3T for all five cases (mean $R2^*$ ratio = 1.8) (please refer to Supporting Table S1 for details), which is in excellent agreement with previous in vivo studies (16,17) as well as theoretical predictions (18).

Because of a potential bias between mGRE and FB-imUTE $T2^*/R2^*$ measurements (due to the employed

sSAT and CHESS pulses), $R2^*$ values obtained with FB-imUTE might not be directly used with existing $R2^*$ -HIC calibrations, which have been exclusively based on mGRE acquisitions (12–15). A systematic comparison of mGRE and FB-imUTE acquisitions in a larger patient cohort could help to provide a $T2^*/R2^*$ correlation. However, the FB-imUTE sequence specifically aims at $T2^*/R2^*$ quantitation in massive iron levels in which existing $R2^*$ -HIC calibrations have shown limited precision (12–15); thus, a new biopsy calibration study will be needed to independently measure reference HIC values and establish a $R2^*$ -HIC calibration at such high HIC levels.

Besides $R2^*$ -based methods for HIC assessment, other approaches such as via liver-to-muscle signal intensity ratio (56) or $T2/R2$ quantitation (57) have been investigated. Liver-to-muscle techniques are based on GRE acquisitions as well (56); thus, their precision also is intrinsically limited in massive iron overload or at higher field strengths. A commercially available $R2^*$ -based method (FerriScan, Resonance Health, Claremont, WA, Australia) offers HIC assessment up to about 43 mg/g dry weight at 1.5T (57), but it might have limited precision for massive HIC levels because the associated $T2$ times will be too short to be reliably detected with

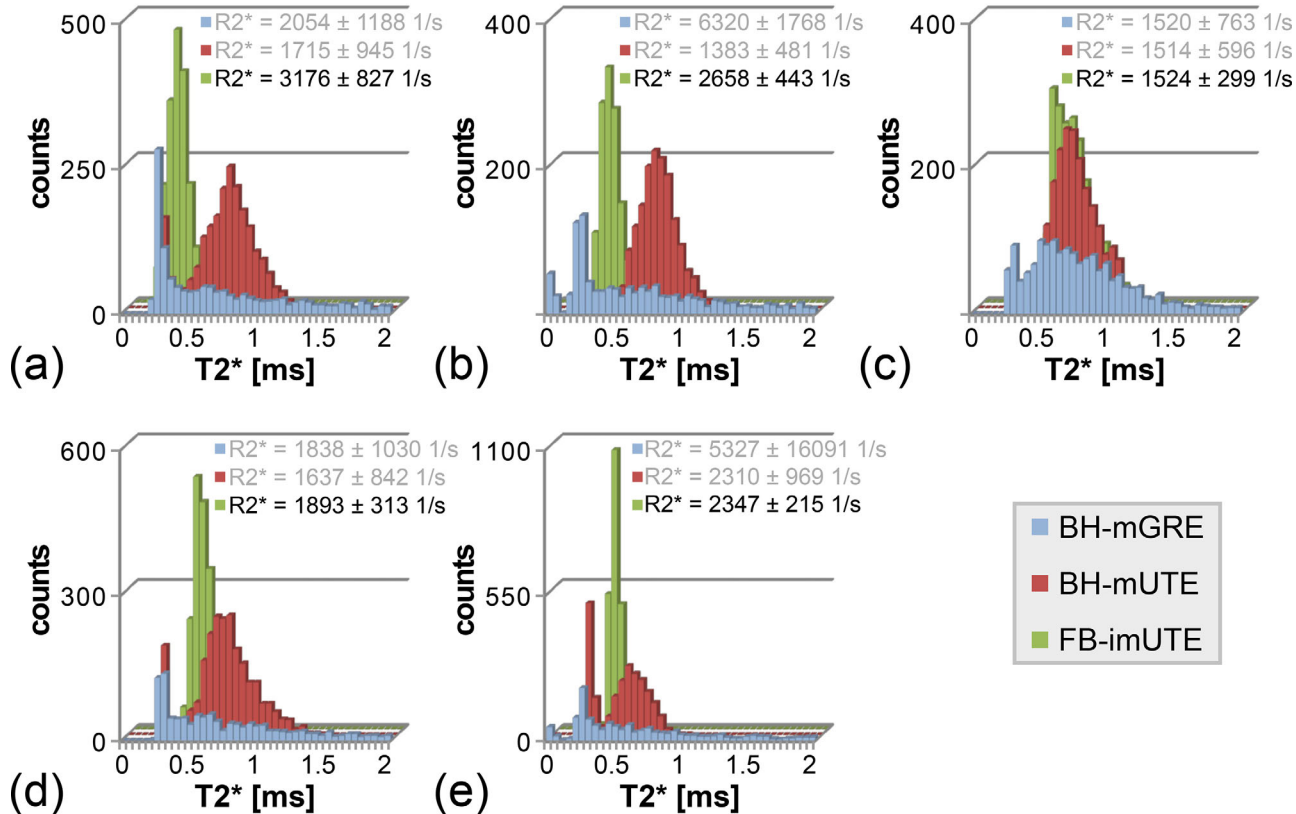


FIG. 8. Histogram plots of the $T2^*$ values found at 3 Tesla in the liver parenchyma after exclusion of unwanted structures for the different sequences. For the two BH sequences, the histogram distribution does not display a clear maximum; thus, mean $R2^*$ quantitation is hampered whereas the FB-imUTE data exhibits a well-defined maximum allowing for a meaningful assessment of mean hepatic $R2^*$. Mean $R2^*$ values (mean \pm standard deviation) of each subject are given in the plot legend for all acquisitions, but only the FB-imUTE sequence gives a trustworthy result.

BH-mGRE, breath-hold multi-gradient echo; BH-mUTE, breath-hold multi-echo ultrashort echo time; FB-imUTE, free-breathing interleaved multi-echo ultrashort echo time; $R2^*$, transverse relaxation rate.

conventional spin-echo sequences. A $T2$ -based calibration for 3T does not exist. The overall lack of a precise MR-based method for HIC estimation in massive iron overload or at 3T might support the need for a new biopsy calibration study in such patients.

The FB-imUTE sequence, presented here, is currently tested in a larger, ongoing clinical trial to systematically compare and evaluate GRE and UTE sequences for $R2^*$ -based assessment of massive HIC at 1.5T and 3T (www.clinicaltrials.gov, NCT01572922). In the study on the general feasibility of 2D UTE imaging in the liver by Chappell et al. (31), the authors also applied fat suppression but did not use additional echo interleaves. The authors did not comment on either implemented mechanisms to counteract slice-selection distortions due to eddy currents or other confounding factors in UTE-based $T2^*$ measurements of the liver. As mentioned in the Introduction, Chappell et al. reported a mean hepatic $T2^*$ value of 7 ms for their hemochromatosis patients, which is substantially longer than the $T2^*$ times of < 1 ms seen in our massive HIC cases. Therefore, some of the pitfalls of UTE-based $T2^*$ quantitation probably were not as apparent in their analysis as in our study, which aims at providing a robust 2D UTE technique to quantify $T2^*/R2^*$ in massive iron overload at both

clinically relevant field strengths. We present the necessary technical developments, which were required to enable quantitative 2D UTE imaging that is not confounded by artifacts from out-of-slice signal contributions or streaking. Proof of concept of the clinical applicability of the FB-imUTE sequence was demonstrated in five subjects with massively high HIC levels.

The current acquisition time of the FB-imUTE sequence of about 1:40 min is longer compared to BH techniques. However, the sequence was well tolerated during in vivo testing because it acquires data in regular free-breathing and does not require any breath-holding or motion-correction concepts (58). The radial sampling pattern makes the FB-imUTE images very robust against respiratory motion. This can be appreciated from Figure 5, which compares images acquired at the first echo time of $TE_1 = 0.1$ ms during breath-holding with the BH-mGRE sequence (Figs. 5f-j) and free-breathing with the FB-imUTE sequence (Figs. 5k-o). Barely any additional artifacts are introduced due to breathing motion. This is in concordance with the pilot work by Chappell et al. (31), in which the authors also report robustness of 2D UTE imaging against abdominal motion, even over the specified acquisition time of about 8.5 min. The motion-insensitivity of radial sampling has been exploited lately

in motion-robust stack-of-stars implementations (59–61) as a powerful alternative to BH acquisitions in patients with impaired BH capabilities. The FB-imUTE capitalizes on the motion insensitivity of radial sampling to collect interleaved echo trains and densely sample the fast signal decay, and thus to improve T₂* quantitation without suffering from degraded image quality due to motion artifacts. Dense temporal sampling could also be achieved by multiple BH-mUTE acquisitions with ΔTE-shifted echo trains in sequential BH maneuvers. However, T₂*/R₂* quantification may be hindered in such an approach by inconsistent BH locations. Continuous free-breathing data acquisition cannot be applied to conventional Cartesian mGRE imaging without motion compensation strategies (58), such as navigator-based concepts, because it would inevitably lead to motion artifacts (62,63) such that hepatic R₂* mapping would be severely hampered.

In the current implementation, image reconstruction was done with Kaiser-Bessel re-gridding techniques. Improved reconstruction strategies such as iterative approaches (64) or compressed sensing (65) might be exploited to achieve a reduction of the total acquisition time via radial data undersampling. As shown in the supporting information, temporal delays between readout gradients and ADC, due to hardware imperfections, have to be accounted for to ensure optimal image quality in radial acquisitions. In our case, a simple, manual approach based on phantom prescans was sufficient to minimize associated image artifacts (please refer to Supporting Figs. S1 and S2 for details). The prescan was only required once per magnet, and the resulting correction times could be maintained during all imaging studies (phantom and *in vivo*). Although this method necessitates another pre-scan for delay adjustment as soon as the sequence is used on different systems, it avoids potentially more complex strategies for delay correction via reconstruction or predistortion of gradient waveforms (44,66–68).

Currently, the FB-imUTE sequence collects all echoes as half echoes, which ensures identical readout conditions for all echoes. Theoretically, fully sampled echoes could be collected for the second and higher echoes of each echo train that would yield higher SNR. We used half-spoke sampling in this initial implementation because half-spoke sampling requires only half the time of fully sampled spokes, which allows for shorter echo spacing. Furthermore, full echo sampling might also require modifications in the T₂* fitting procedure to account for differences in the noise level of half and full echoes. A reduction of the echo spacing within one interleave (currently 1.8 ms) could also be achieved by using a smaller readout matrix size (eg, 64). This would, however, lead to a lower spatial resolution. Although larger voxel sizes would also yield higher SNR, the spatial resolution still has to be high enough to clearly distinguish, for example, blood vessels from liver parenchyma, which is important to avoid contamination of the hepatic T₂* assessment due to partial volume effects. Nevertheless, both concepts—a full echo acquisition for second and higher echoes and a reduced readout matrix size—could be investigated to optimize SNR and scan time in the future.

A potential limitation of the FB-imUTE sequence is that the half-pulse excitation, together with the application of sSAT bands, limits its multi-slice capability. The sequence only provides data from a single plane and does not cover the whole liver. Multiple slices could be measured via sequential acquisitions or in an interleaved fashion if the slices are separated by the width of the sSAT bands, but both strategies may not be advantageous from a total scan time perspective. However, existing R₂*-HIC calibrations have been established for single-slice mGRE acquisitions through the center of the liver (12–15) such that a single plane seems to be sufficient for HIC assessment.

CONCLUSION

In summary, the lack of precision of R₂*-based HIC assessment with mGRE methods poses shortcomings in the clinical management of patients with massive iron overload. In previous studies, about 40% of patients with iron overload showed HIC levels of 15 mg Fe/g dry weight or more (13,14). Current mGRE techniques are intrinsically limited when detecting signals from tissues with short T₂* times on the scale of 1 ms or less, which corresponds to HIC levels above approximately 25 mg Fe/g dry weight at 1.5T and 12.5 mg Fe/g dry weight at 3T. We conclude that the proposed UTE sequence offers the opportunity to provide a means of precisely measuring T₂*/R₂* in iron-overloaded patients over the entire clinically relevant HIC range at 1.5T and 3T (including massive iron overload settings). This is achieved by incorporating sequence modules which minimize out-of-slice signal contribution and streaking artifacts and can be easily implemented on any scanner. Before clinical adoption of these methods, it will be necessary to perform a thorough biopsy-referenced trial. Such a systematic clinical study currently is underway.

ACKNOWLEDGMENTS

The authors would like to acknowledge Gail Fortner, RN, Karen Wodowski, PNP, and Darla Pickett, PA-C, MHS, for patient recruitment and enrollment; Kamisha Flowers, BS, for managing regulatory aspects of the study; and Robert Gold, MD, and Kimberly Proctor, PNP, for performing liver biopsies (all from St. Jude Children's Research Hospital, Memphis, TN). The authors are indebted to Raymond Osarogiagbon, MD, and Laura M. McHugh, RN (both from Baptist Memorial Hospital, Memphis, TN); and Patricia Adams-Graves, MD, Vanessa Steele, MSW, and Angela Hudson, FNP (all three from Regional One Health, Memphis, TN), for support with patient recruitment. The authors would also like to thank Dr. Mark Bydder (University of California, San Diego, CA) for support with implementation of image reconstruction.

Parts of this study were presented as an oral contribution (abstract number: 87) at the 23rd Annual Meeting of the International Society for MRM in Toronto, Ontario, Canada, 30 May - 5 June 2015.

REFERENCES

1. Taher AT, Musallam KM, Inati A. Iron overload: consequences, assessment, and monitoring. *Hemoglobin* 2009;33(suppl 1):S46–S57.
2. Kohgo Y, Ikuta K, Ohtake T, Torimoto Y, Kato J. Body iron metabolism and pathophysiology of iron overload. *Int J Hematol* 2008;88:7–15.
3. Olynyk JK, St Pierre TG, Britton RS, Brunt EM, Bacon BR. Duration of hepatic iron exposure increases the risk of significant fibrosis in hereditary hemochromatosis: a new role for magnetic resonance imaging. *Am J Gastroenterol* 2005;100:837–841.
4. Harmatz P, Butensky E, Quirolo K, Williams R, Ferrell L, Moyer T, Golden D, Neumayr L, Vichinsky E. Severity of iron overload in patients with sickle cell disease receiving chronic red blood cell transfusion therapy. *Blood* 2000;96:76–79.
5. Angelucci E, Brittenham GM, McLaren CE, Ripalti M, Baronciani D, Giardini C, Galimberti M, Polchi P, Lucarelli G. Hepatic iron concentration and total body iron stores in thalassemia major. *N Engl J Med* 2000;343:327–331.
6. Olivieri NF. Progression of iron overload in sickle cell disease. *Semin Hematol* 2001;38:57–62.
7. Prati D, Maggioni M, Milani S, et al. Clinical and histological characterization of liver disease in patients with transfusion-dependent beta-thalassemia. A multicenter study of 117 cases. *Haematologica* 2004;89:1179–1186.
8. Brittenham GM, Griffith PM, Nienhuis AW, McLaren CE, Young NS, Tucker EE, Allen CJ, Farrell DE, Harris JW. Efficacy of deferoxamine in preventing complications of iron overload in patients with thalassemia major. *N Engl J Med* 1994;331:567–573.
9. Ladis V, Chouliaras G, Berdousi H, Kanavakis E, Kattamis C. Longitudinal study of survival and causes of death in patients with thalassemia major in Greece. *Ann N Acad Sci* 2005;1054:445–450.
10. Sirlin CB, Reeder SB. Magnetic resonance imaging quantification of liver iron. *Magn Reson Imaging Clin N Am* 2010;18:359–381, ix.
11. Angelucci E, Baronciani D, Lucarelli G, et al. Needle liver biopsy in thalassaemia: analyses of diagnostic accuracy and safety in 1184 consecutive biopsies. *Br J Haematol* 1995;89:757–761.
12. Anderson LJ, Holden S, Davis B, et al. Cardiovascular T2-star (T2*) magnetic resonance for the early diagnosis of myocardial iron overload. *Eur Heart J* 2001;22:2171–2179.
13. Wood JC, Enriquez C, Ghugre N, Tyzka JM, Carson S, Nelson MD, Coates TD. MRI R2 and R2* mapping accurately estimates hepatic iron concentration in transfusion-dependent thalassemia and sickle cell disease patients. *Blood* 2005;106:1460–1465.
14. Hankins JS, McCarville MB, Loeffler RB, Smeltzer MP, Onciu M, Hoffer FA, Li CS, Wang WC, Ware RE, Hillenbrand CM. R2* magnetic resonance imaging of the liver in patients with iron overload. *Blood* 2009;113:4853–4855.
15. Henninger B, Zoller H, Rauch S, Finkenstedt A, Schocke M, Jaschke W, Kremsner C. R2* relaxometry for the quantification of hepatic iron overload: biopsy-based calibration and comparison with the literature. *Rofo* 2015;187:472–479.
16. Storey P, Thompson AA, Carqueville CL, Wood JC, de Freitas RA, Rigsby CK. R2* imaging of transfusional iron burden at 3T and comparison with 1.5T. *J Magn Reson Imaging* 2007;25:540–547.
17. Hillenbrand CM, Loeffler RB, McCarville MB, et al. Evaluation of hepatic iron concentrations by R2* magnetic resonance imaging in 35 patients with iron overload: comparison of R2* measurements at 1.5T and 3T and validation with liver biopsies. In Proceedings of the 16th Annual Meeting of ISMRM, Toronto, Canada, 2008. Abstract 90.
18. Ghugre NR, Doyle EK, Storey P, Wood JC. Relaxivity-iron calibration in hepatic iron overload: Predictions of a Monte Carlo model. *Magn Reson. Med.* 2015;74:879–883.
19. Robson MD, Gatehouse PD, Bydder M, Bydder GM. Magnetic resonance: an introduction to ultrashort TE (UTE) imaging. *J Comput Assist Tomogr* 2003;27:825–846.
20. Bergin CJ, Pauly JM, Macovski A. Lung parenchyma: projection reconstruction MR imaging. *Radiology* 1991;179:777–781.
21. Ohno Y, Koyama H, Yoshikawa T, Matsumoto K, Takahashi M, Van Cauteren M, Sugimura K. T2* measurements of 3-T MRI with ultrashort TE: capabilities of pulmonary function assessment and clinical stage classification in smokers. *Am J Roentgenol* 2011;197:W279–W285.
22. Robson MD, Bydder GM. Clinical ultrashort echo time imaging of bone and other connective tissues. *NMR Biomed* 2006;19:765–780.
23. Serai SD, Laor T, Dwek JR, Zbojnewicz AM, Carl M. Feasibility of ultrashort TE (UTE) imaging of children at 1.5 T. *Pediatr Radiol* 2014;44:103–108.
24. Du J, Carl M, Bydder M, Takahashi A, Chung CB, Bydder GM. Qualitative and quantitative ultrashort echo time (UTE) imaging of cortical bone. *J Magn Reson* 2010;207:304–311.
25. Biswas R, Bae W, Diaz E, Masuda K, Chung CB, Bydder GM, Du J. Ultrashort echo time (UTE) imaging with bi-component analysis: bound and free water evaluation of bovine cortical bone subject to sequential drying. *Bone* 2012;50:749–755.
26. Du J, Bydder GM. Qualitative and quantitative ultrashort-TE MRI of cortical bone. *NMR Biomed* 2013;26:489–506.
27. Du J, Sheth V, He Q, Carl M, Chen J, Corey-Bloom J, Bydder GM. Measurement of T1 of the Ultrashort T2* Components in White Matter of the Brain at 3T. *PLOS ONE* 2014;9:e103296.
28. Du J, Ma G, Li S, Carl M, Szeverenyi NM, Vandenberg S, Corey-Bloom J, Bydder GM. Ultrashort echo time (UTE) magnetic resonance imaging of the short T2 components in white matter of the brain using a clinical 3T scanner. *Neuroimage* 2014;87:32–41.
29. Wansapura JP, Daniel BL, Pauly J, Butts K. Temperature mapping of frozen tissue using eddy current compensated half excitation RF pulses. *Magn Reson Med* 2001;46:985–992.
30. Lu A, Daniel BL, Pauly JM, Butts Pauly K. Improved slice selection for R2* mapping during cryoablation with eddy current compensation. *J Magn Reson Imaging* 2008;28:190–198.
31. Chappell KE, Patel N, Gatehouse PD, Main J, Puri BK, Taylor-Robinson SD, Bydder GM. Magnetic resonance imaging of the liver with ultrashort TE (UTE) pulse sequences. *J Magn Reson Imaging* 2003;18:709–713.
32. Pauly JM, Conolly S, Nishimura D, Macovski A. Slice-selective excitation for very short T2 species. In Proceedings of the 8th Annual SMRM Meeting, Amsterdam, The Netherlands, 1989. p. 28.
33. Pauly JM. Selective excitation for ultrashort echo time imaging. *eMagRes* 2012. doi: 10.1002/9780470034590.emrstm1271.
34. Tyler DJ, Robson MD, Henkelman RM, Young IR, Bydder GM. Magnetic resonance imaging with ultrashort TE (UTE) PULSE sequences: technical considerations. *J Magn Reson Imaging* 2007;25:279–289.
35. Josan S, Pauly JM, Daniel BL, Pauly KB. Double half RF pulses for reduced sensitivity to eddy currents in UTE imaging. *Magn Reson Med* 2009;61:1083–1089.
36. Josan S, Kaye E, Pauly JM, Daniel BL, Pauly KB. Improved half RF slice selectivity in the presence of eddy currents with out-of-slice saturation. *Magn Reson Med* 2009;61:1090–1095.
37. Harkins KD, Horch RA, Does MD. Simple and robust saturation-based slice selection for ultrashort echo time MRI. *Magn Reson Med* 2015;73:2204–2211.
38. Hargreaves BA, Cunningham CH, Nishimura DG, Connelly SM. Variable-rate selective excitation for rapid MRI sequences. *Magn Reson Med* 2004;52:590–597.
39. Block KT, Chandarana H, Milla S, et al. Towards routine clinical use of radial stack-of-stars 3D gradient-echo sequences for reducing motion sensitivity. *J Korean Soc Magn Reson Med* 2014;18:87–106.
40. Haase A, Frahm J, Hanicke W, Matthaei D. 1H NMR chemical shift selective (CHESS) imaging. *Phys Med Biol* 1985;30:341–344.
41. Glover GH, Pauly JM. Projection reconstruction techniques for reduction of motion effects in MRI. *Magn Reson Med* 1992;28:275–289.
42. Jackson JI, Meyer CH, Nishimura DG, Macovski A. Selection of a convolution function for Fourier inversion using gridding [computerised tomography application]. *IEEE Trans Med Imaging* 1991;10:473–478.
43. Pipe JG, Menon P. Sampling density compensation in MRI: rationale and an iterative numerical solution. *Magn Reson Med* 1999;41:179–186.
44. Peters DC, Derbyshire JA, McVeigh ER. Centering the projection reconstruction trajectory: reducing gradient delay errors. *Magn Reson Med* 2003;50:1–6.
45. Feng Y, He T, Gatehouse PD, Li X, Harith Alam M, Pennell DJ, Chen W, Firmin DN. Improved MRI R2 * relaxometry of iron-loaded liver with noise correction. *Magn Reson Med* 2013;70:1765–1774.
46. McCarville MB, Hillenbrand CM, Loeffler RB, Smeltzer MP, Song R, Li CS, Hankins JS. Comparison of whole liver and small region-of-interest measurements of MRI liver R2* in children with iron overload. *Pediatr Radiol* 2010;40:1360–1367.
47. Scheffler K, Hennig J. Reduced circular field-of-view imaging. *Magn Reson Med* 1998;40:474–480.
48. Block KT, Fenchel M. Simple method for attenuation of streaking artifacts from peripheral intensity accumulation. In Proceedings of

- the 20th Annual Meeting of ISMRM, Melbourne, Australia, 2012. Abstract 2444.
49. Xue Y, Yu J, Kang HS, Englander S, Rosen MA, Song HK. Automatic coil selection for streak artifact reduction in radial MRI. *Magn Reson Med* 2012;67:470–476.
 50. Kholmovski EG, Parker DL, Di Bella EV. Streak artifact suppression in multi-coil MRI with radial sampling. In Proceedings of the 15th Annual Meeting of ISMRM, Berlin, Germany, 2007. Abstract 1902.
 51. Bley TA, Wieben O, Francois CJ, Brittain JH, Reeder SB. Fat and water magnetic resonance imaging. *J Magn Reson Imaging* 2010;31:4–18.
 52. Hu HH, Bornert P, Hernando D, Kellman P, Ma J, Reeder S, Sirlin C. ISMRM workshop on fat-water separation: insights, applications and progress in MRI. *Magn Reson Med* 2012;68:378–388.
 53. Meloni A, Tyszka JM, Pepe A, Wood JC. Effect of inversion recovery fat suppression on hepatic R2* quantitation in transfusional siderosis. *AJR Am J Roentgenol* 2015;204:625–629.
 54. Krafft AJ, Loeffler RB, Song R, Bian X, McCarville MB, Hankins JS, Hillenbrand CM. Does fat suppression via chemically selective saturation affect R2*-MRI for transfusional iron overload assessment? A clinical evaluation at 1.5T and 3T. *Magn Reson Med* 2016;76:591–601.
 55. Henkelman RM, Stanisz GJ, Graham SJ. Magnetization transfer in MRI: a review. *NMR Biomed* 2001;14:57–64.
 56. Gandon Y, Olivie D, Guyader D, Aube C, Oberti F, Sebille V, Deugnier Y. Non-invasive assessment of hepatic iron stores by MRI. *Lancet* 2004;363:357–362.
 57. St Pierre TG, Clark PR, Chua-Anusorn W, Fleming AJ, Jeffrey GP, Olynyk JK, Pootrakul P, Robins E, Lindeman R. Noninvasive measurement and imaging of liver iron concentrations using proton magnetic resonance. *Blood* 2005;105:855–861.
 58. Zaitsev M, Maclarens J, Herbst M. Motion artifacts in MRI: a complex problem with many partial solutions. *J Magn Reson Imaging* 2015;42:887–901.
 59. Azevedo RM, de Campos RO, Ramalho M, Heredia V, Dale BM, Semelka RC. Free-breathing 3D T1-weighted gradient-echo sequence with radial data sampling in abdominal MRI: preliminary observations. *AJR Am J Roentgenol* 2011;197:650–657.
 60. Chandarana H, Block TK, Rosenkrantz AB, Lim RP, Kim D, Mossa DJ, Babb JS, Kiefer B, Lee VS. Free-breathing radial 3D fat-suppressed T1-weighted gradient echo sequence: a viable alternative for contrast-enhanced liver imaging in patients unable to suspend respiration. *Invest Radiol* 2011;46:648–653.
 61. Chandarana H, Block KT, Winfield MJ, Lala SV, Mazori D, Giuffrida E, Babb JS, Milla SS. Free-breathing contrast-enhanced T1-weighted gradient-echo imaging with radial k-space sampling for paediatric abdominopelvic MRI. *Eur Radiol* 2014;24:320–326.
 62. Axel L, Summers RM, Kressel HY, Charles C. Respiratory effects in two-dimensional Fourier transform MR imaging. *Radiology* 1986;160:795–801.
 63. Wood ML, Henkelman RM. MR image artifacts from periodic motion. *Med Phys* 1985;12:143–151.
 64. Block KT, Uecker M, Frahm J. Undersampled radial MRI with multiple coils. Iterative image reconstruction using a total variation constraint. *Magn Reson Med* 2007;57:1086–1098.
 65. Lustig M, Donoho D, Pauly JM. Sparse MRI: the application of compressed sensing for rapid MR imaging. *Magn Reson Med* 2007;58:1182–1195.
 66. Moussavi A, Untenberger M, Uecker M, Frahm J. Correction of gradient-induced phase errors in radial MRI. *Magn Reson Med* 2014;71:308–312.
 67. Kramer M, Biermann J, Reichenbach JR. Intrinsic correction of system delays for radial magnetic resonance imaging. *Magn Reson Imaging* 2015;33:491–496.
 68. Harkins KD, Does MD, Grissom WA. Iterative method for predistortion of MRI gradient waveforms. *IEEE Trans Med Imaging* 2014;33:1641–1647.

SUPPORTING INFORMATION

Additional supporting information may be found in the online version of this article.

Fig. S1. Manual correction of delay parameters between readout gradient and ADC due to system imperfections. (a) UTE image after delay adjustment. (b) Delay parameter too short – artifacts emerge as dark rim (red arrow). (c) Delay parameter too long – artifacts emerge as bright rim (green arrow). For illustration purposes, the delays in (b) and (c) were deliberately adjusted to yield a symmetric artifact shape. (d) Intensity profiles along the horizontal axis (x-axis) through the center of phantom (indicated by blue (a), red (b), and green (c) lines). After correction for temporal delays, a uniform intensity profile is seen (blue).

Fig. S2. Iterative, manual adjustment of delay parameters in a series of axial phantom pre-scans. The delay parameters can be adjusted independently for each physical gradient direction (here x- and y-gradient direction). (a) Adjustment delay parameter for x-gradient direction. (b) Adjustment of y-gradient. The UTE image in the middle of each row represents the image with correctly adjusted delay parameters.

Table S1. Summary of mean hepatic R2* values measured at 1.5T and 3T with the BH-mGRE, BH-mUTE, and FB-imUTE sequences for the five subjects with massive hepatic iron content together with the respective R2* ratios. Mean R2* values are given with the physical unit [1/s] together with their standard deviation (mean \pm standard deviation).